J. Fluid Mech. (2018), *vol.* 851, *pp.* 715–738. © Cambridge University Press 2018
doi:10.1017/jfm.2018.509

Viscous constraints on microorganism approach and interaction

Mehdi Jabbarzadeh[1] **and Henry Chien Fu**[1,†]

[1]Department of Mechanical Engineering, University of Utah, Salt Lake City, UT 84112, USA

(Received 2 February 2018; revised 18 May 2018; accepted 19 June 2018;
first published online 31 July 2018)

Microorganisms must approach other suspended organisms or particles in order to interact with them during a host of life processes including feeding and mating. Microorganisms live at low Reynolds number where viscosity dominates and strongly affects the hydrodynamics of swimmer and nearby cells and objects. Viscous hydrodynamics makes it difficult for two surfaces to approach closely at low Reynolds numbers. Nonetheless, it is observed that microorganisms in fluid are still able to approach closely enough to interact with each other or suspended particles. Here, we study how the physical constraints provided by viscous hydrodynamics affects the feasibility of direct approach of flagellated and ciliated microorganisms to targets of different sizes. We find that it is feasible for singly flagellated swimmers to approach targets that are the same size or bigger. On the other hand, for squirmers, the feasibility of approach depends on near-field flows that can be controlled by the details of their swimming strokes.

Key words: biological fluid dynamics, micro-organism dynamics, swimming/flying

1. Introduction

Microorganisms live in viscous environments in which they interact with other organisms for genetic exchange, mating and colonization, as well as interact with other nearby passive and active particles that are prey or nutrient sources (Lauga & Powers 2009). These interactions are crucial for enhancing populations, establishing a community during colonization, biofilm formation and microbe–host interactions (Braga, Dourado & Araújo 2016). Many of these interactions require inducing near contact between the microorganism and target (either another microorganism or a particle) in a viscous flow, and can involve a wide range of swimmer and target particle sizes. For example, during feeding the size of prey is generally much smaller than the predator (Hansen, Bjornsen & Hansen 1994; Kiørboe *et al.* 2009; Riisgård & Larsen 2010; Kiørboe 2016; Johnke *et al.* 2017; Sommer *et al.* 2017). However, during bacterial conjugation (Griffiths *et al.* 2000), zooplankton mating (Strickler 1998; Kiørboe 2007) or colonization an organism approaches another member of the same species of similar size. Approach to larger targets also occurs during fertilization of an egg by sperm (Moreno *et al.* 2011) or when bacteria find new

† Email address for correspondence: henry.fu@utah.edu

https://doi.org/10.1017/jfm.2018.509 Published online by Cambridge University Press

habitats by approaching marine snow, small biological debris which provides a local nutrient source and habitat in the ocean (Kiørboe *et al.* 2003; Grossart *et al.* 2006).

The microorganisms we study live at low Reynolds number (10^{-5}–10^{-1}) where there is a thick boundary layer of fluid that moves together with their moving body or appendages. This hydrodynamic boundary layer plays an important role in the hydrodynamic interactions of a swimmer and other particles, and makes it difficult to closely approach target particles. For example, when a copepod feeds on a particle, the movements of its appendages induce hydrodynamic flows that tend to push or pull the particle in concert with the appendage (Koehl & Strickier 1981), and due to the kinematic reversibility of flows at low Reynolds number it is difficult for the copepod to easily move the particle closer to its mouth.

Small target particles near a swimming microorganism are often assumed to follow streamlines of the flow induced by the swimmer in the absence of other particles. However, understanding approach to similarly or larger-sized particles, or understanding very close approach to particles of any size, requires incorporating the hydrodynamic interactions between the microorganism and target. Although microorganisms (including their appendages) and targets can have complex shapes, physical insight into their hydrodynamic interactions can be gained by considering analytically tractable geometries such as approaching spheres. The exact solution for the motion of two spheres translating with the same velocity along their common diameter was first developed by Stimson & Jeffery (1926). The special case of a sphere approaching a solid plane was extensively studied (Brenner 1961; Cox & Brenner 1967) for both large separations and close to contact. Later, Ishikawa, Simmonds & Pedley (2006) analytically calculated the interaction of two spherical 'squirmer' swimmers, both in the limit of small separation using lubrication theory, and in the limit of large separation using a multipole expansion, then compared their results with numerical (boundary element method) simulations. Potomkin *et al.* (2013) discuss the collision (i.e. physical contact) of microswimmers with different boundary conditions in a viscous fluid. They show that with no-slip boundary conditions collisions between two swimmers are impossible in finite collision times, while with slip boundaries collisions can occur within finite times. Li, Ostace & Ardekani (2016) numerically investigate the inertial effects on hydrodynamic interaction of squirming organisms and show that these inertial effects greatly affect the interaction of organisms. More recently, Shaik & Ardekani (2017) discuss the motion of squirmer microorganisms near weakly deformable interfaces using the method of reflections. Papavassiliou & Alexander (2017) also found an exact solution for the hydrodynamic interactions of two squirmers, and provide exact solution for specific cases when the squirmer sphere is close to a solid or free surface to study hydrodynamic interactions of swimmers in confined boundaries.

In this paper, we investigate the physical constraints placed by viscous hydrodynamics on organisms approaching passive target particles. We first review the exact solution for two spheres with no-slip boundaries in a bispherical coordinate system described in Stimson & Jeffery (1926). As a simple example of hydrodynamic constraints on approach, in § 2 we modify this solution for the case when the two spheres have different velocities and one sphere is pushed by a constant, localized propulsion force towards the other sphere which is a neutrally buoyant (force-free) target. To show that the physical insights from this model also apply to swimmers, in § 2.2 we validate a numerical method for studying close approach and use it to study a singly flagellated swimmer with spherical cell body approaching a spherical target. For both of these cases with localized propulsion, we find that approach is feasible

https://doi.org/10.1017/jfm.2018.509 Published online by Cambridge University Press

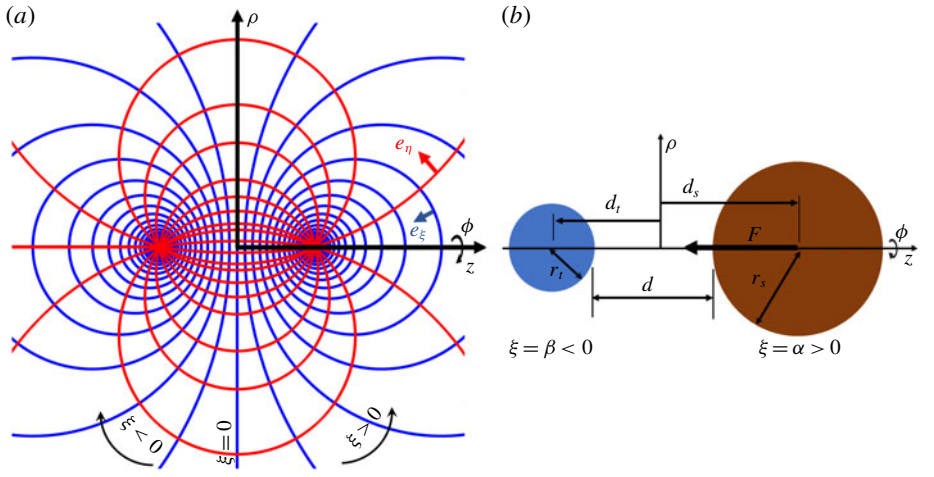


FIGURE 1. (Colour online) (*a*) Relation between the bispherical coordinate system (ξ, η, ϕ) and cylindrical coordinate system (z, ρ, ϕ). The axisymmetric ϕ coordinate is rotation about the z-axis. (*b*) Spherical swimmer with radius r_s is pushed by a constant force ($\boldsymbol{F} = F_s\hat{\boldsymbol{z}} = -F\hat{\boldsymbol{z}}$) toward a force free spherical target particle with radius r_t. The surface-to-surface separation distance of the swimmer and particle is d and surfaces with constant ξ describe spheres in bispherical coordinate system for the swimmer ($\xi = \alpha > 0$) and target ($\xi = \beta < 0$).

when the target is of similar or larger size than the swimmer, but much less feasible for smaller size targets. Finally, to study organisms with distributed propulsion, in § 3 we provide results from exact solutions for a spherical squirmer approaching a no-slip target sphere in the bispherical coordinate system. We find that swimmers with distributed propulsion mechanisms can generate currents during swimming that allow them to approach smaller as well as larger targets, with differences in the currents and approach feasibility controlled by details of the swimmer's stroke.

2. Approach with localized propulsion

2.1. *Analytical model for approaching spheres – localized propulsion*

We developed an analytical model for the approach of two spheres along their centreline in Stokes flow. The spherical swimmer is assumed to be pushed toward a force-free suspended spherical target particle by a constant force F along their common centreline (figure 1*b*). Although swimming microorganisms should be considered force free, as we show in § 2.2, this simple model has similar qualitative features to a force-free swimmer with a single localized propulsion element, with the constant force corresponding to the localized thrust on the body provided by the element. Note that the 'swimming' sphere could also be a model for an appendage or a portion of an organism, in which case the constant force would describe the force exerted on it by the rest of the organism. Also, note that a number of real organisms do have roughly spherical geometries, such as *Opalina* and *Volvox* (Ishikawa *et al.* 2006).

Our solution is based on finding the Stokes streamfunction in the bispherical coordinate system (figure 1*a*) for an axisymmetric Stokes flow around the spheres. Stimson & Jeffery (1926) found the solution for spheres translating along their

https://doi.org/10.1017/jfm.2018.509 Published online by Cambridge University Press

common centreline with the same velocities. Here, we straightforwardly extend their solution so that spheres can have different velocities during their interactions along their centreline. The details of our solution are described in appendix A. As expected from Stokesian dynamics, the velocities are linear in the forces on each sphere and are related by the resistance matrix ($[F_s;\ F_t] = \boldsymbol{R}[V_s;\ V_t]$). For our model, we are interested in the approach dynamics when the swimmer is pushed by a constant propulsion force ($\boldsymbol{F} = F_s\hat{\boldsymbol{z}} = -F\hat{\boldsymbol{z}}$) towards the target, and the target has zero force ($F_t = 0$). Note that for given sphere sizes, the resistance matrix $\boldsymbol{R}$ depends on the separation of spheres and must be recalculated at each time during their approach. Inverting $\boldsymbol{R}$, we solve for the sphere velocities at each time step, and integrate to find sphere trajectories assuming an initial separation d_0.

The no-collision paradox indicates that it would take infinite time for the swimmer to physically contact the target particle in a viscous flow (Potomkin *et al.* 2013). However, since organisms can get close enough to interact, rather than using a criterion of physical contact ($d = 0$), we arbitrarily choose a cutoff and deem a separation of a hundredth of the swimmer radius ($d = 0.01r_s$) as 'close enough' approach. Physically, the idea is that at shorter distances (e.g. $0.01r_s \approx 10$ nm for a bacterium) non-hydrodynamic interactions such as electrostatic, van der Waals or biochemical bonding, will become important and take over to enable predation, capture or adhesion. Typical approach trajectories, separations and velocities are shown in figures 2(*a*,*b*) for the same size of the swimmer and target particle ($r = 1$). We set the initial separation of the swimmer and target spheres to be 10 times of the swimmer radius for all calculations ($d_0 = 10r_s$). For large separations (i.e. at early times), the swimmer easily gets closer to the target particle at a rate corresponding to its interaction-free swimming speed $V_0 = F/(6\pi\mu r_s)$ (given by the Stokes drag formula for an isolated sphere), but when the swimmer gets closer to the target, hydrodynamic interactions push the target away from the swimmer and the target velocity approaches the swimmer velocity as the separation decreases. Accordingly, the rate of decrease of the separation distance d also decreases. We can delineate a highly hydrodynamically interacting regime when the approach velocity is less than half the initial value (dotted vertical line in figure 2), which starts to occur at a separation distance of approximately the size of the swimmer.

To characterize the feasibility of approach, we measure the total distance ΔS necessary for the swimmer to travel before approaching within the cutoff separation ($d = 0.01r_s$). Unlike measures such as time of approach, the total distance ΔS is a kinematic parameter which does not depend on the input power (or external force F_s) of the swimmer. The results are shown in figure 3(*b*) for different target : swimmer size ratios (blue line and square symbols). For target particles of similar size or larger than the swimmer, the swimmer does not have to travel much more than the initial distance d_0 (for $r_t/r_s = 10$, $\Delta S = 1.04d_0$ and for $r_t/r_s = 1$, $\Delta S = 1.53d_0$) since the target does not move much, and approach is feasible. On the other hand, for smaller targets, the target is pushed away by a significant amount and the swimmer has to travel farther (up to approximately $8\times$ the initial separation distance), so approach is less feasible.

These results suggest that swimmers using localized propulsion can directly approach similarly sized objects, which happens during mating or conjugation. In addition, such swimmers can approach much bigger particles, which happens when bacteria approach marine snow to find new environments ($r_t/r_s \geqslant 10$–100), or sperm fertilizes an egg ($r_t/r_s \approx 20$ for humans (Alberts *et al.* 2002)). However, they may have trouble directly approaching or manipulating particles that are small compared

https://doi.org/10.1017/jfm.2018.509 Published online by Cambridge University Press

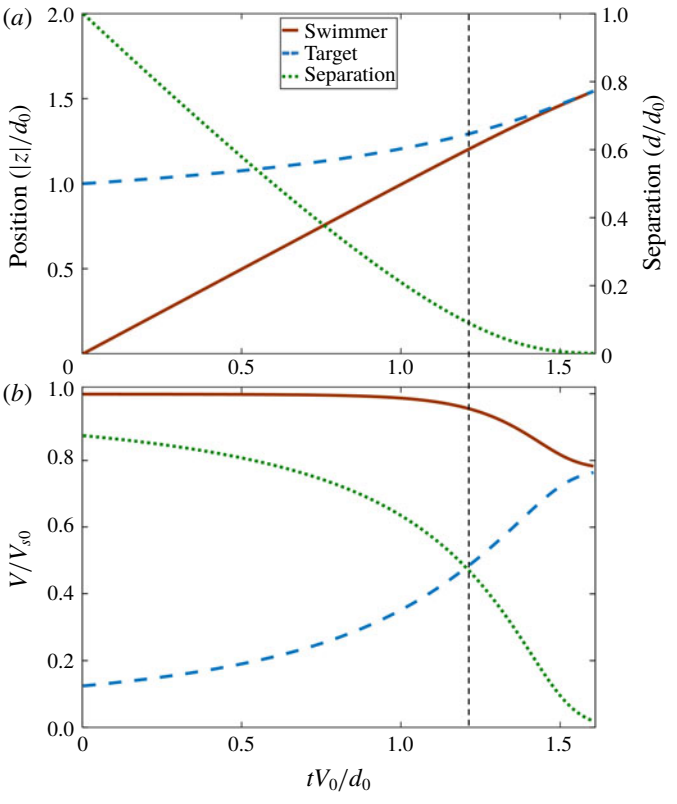


FIGURE 2. (Colour online) (*a*) Typical trajectory and separation of the swimmer and target particle over time for $r_s/r_t = 1$. (*b*) Velocities of the swimmer and target particle and the rate of change of the separation normalized by the interaction-free swimming speed $V_0 = F/(6\pi\mu r_s)$. The particle starts to move with small velocity at the initial separation of $d_0 = 10r_s$, the target moves with small velocity, but when the separation is less than about the swimmer size (vertical dashed line), hydrodynamic interactions cause the target to move away from the swimmer, so the rate of change of separation decreases.

to the swimmer size, which happens in feeding processes (e.g. $r_t/r_s \approx 0.05$ for a copepod feeding on zooplankton). If the appendages are used to approach a target, those appendages should be of similar size or smaller than the target. For example, during conjugation a much smaller pilus can extend between two bacteria.

2.2. *Numerical model for flagellated microswimmers – localized propulsion*

The results of the previous section suggest how hydrodynamic interactions may place constraints on the ability of microorganisms to closely approach other particles. However, unlike real microswimmers, the swimmer model we used was not force and torque free. In this section, we numerically examine the approach of a singly flagellated force- and torque-free microswimmer toward a suspended target particle to confirm that the physical conclusions from the simple model remain valid.

We model hydrodynamic contributions of the spherical cell body and target particle by the boundary element method (BEM) (Phan-Thien, Tran-Cong & Ramia 1987; Ramia, Tullock & Phan-Thien 1993; Smith 2009), and model hydrodynamic

https://doi.org/10.1017/jfm.2018.509 Published online by Cambridge University Press

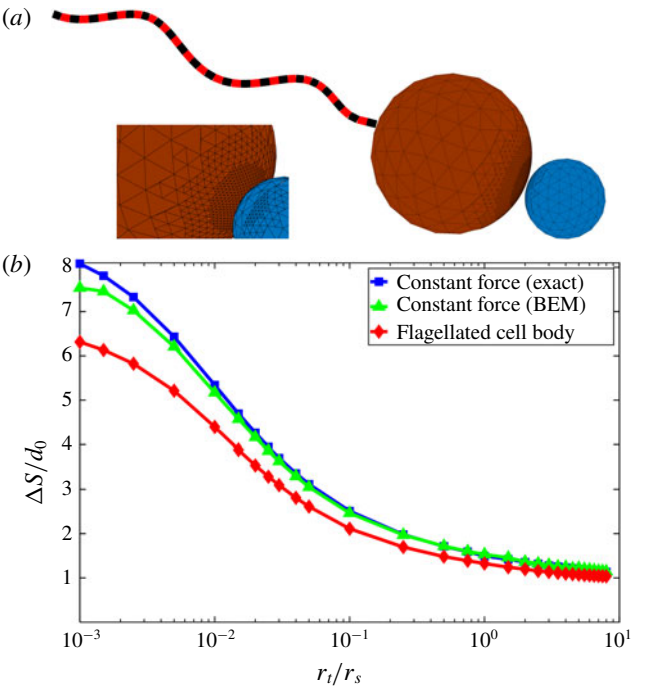


FIGURE 3. (Colour online) (*a*) Adaptive discretization of the swimmer cell body and target particle with surface triangular elements used for the boundary element method (BEM), and discretization for the swimmer flagellum used for slender body theory (SBT). (*b*) Total travelled distance ΔS required for the swimmer to approach within $0.01r_s$ of the target after starting from initial separation of $10r_s$, as a function of target : swimmer size ratios. Analytical solution (blue squares) for two spheres (as in § 2) validates numerical results for the same situation obtained by BEM (green triangles). BEM results for the single-flagellated model (red diamonds) are qualitatively similar to the constant force case.

contributions of the slender flagellum by slender body theory (SBT) (Higdon 1979). The details and formulation of the numerical method are described in appendix B.

To validate our numerical method, we compare numerical results for a sphere pushed by an external force without a flagellum towards a target sphere (figure 3*b* – green triangles) with the analytical solutions from § 2 (figure 3*b* – blue squares). Relative to the exact solutions, we find 1 % average errors for the numerics arising from discretization and quadrature. The error is less than 2 % for size ratios bigger than 0.01, while it is approximately 7 % for the smallest size ratio of 0.001.

We compare the travel distance needed for the swimmer to approach within the cutoff distance $d = 0.01r_s$ of the target particle for the single-flagellated swimmer and constant force case in figure 3(*b*) (red diamond). The comparison shows that both cases have qualitatively the same trend – for small target spheres, a swimmer must move very far to catch the target particle, but for similar size or larger targets, the swimmer does not need to move much farther than the initial separation distance. Quantitatively, the difference between these two cases is an approximately constant factor of 10–15 % in travelled distance for the swimmer. Thus, for the purposes of approach, one can model a flagellated swimmer with localized propulsion as a body pushed by constant force. The simple physical explanation for this is that the slender

https://doi.org/10.1017/jfm.2018.509 Published online by Cambridge University Press

flagellum rotates behind the cell body and most of the hydrodynamic interactions are between the cell body and the target rather than the flagellum and the target. Note that this also implies that varying the geometry of the flagellum will not have large effects on the travel distance ΔS.

3. Approach with distributed propulsion

The previous results model microorganisms that swim using localized propulsion methods, such as a single flagellum, and suggest that approach towards smaller target particles such as prey is less feasible. However, many zooplankton use distributed propulsion generated by numerous appendages or cilia, and these organisms have been observed to feed by capturing prey using feeding currents. For instance, paramecia use beating cilia to capture food particles and transport these particles to their mouths (Balazs *et al.* 2014). This suggests that the use of distributed flow sources such as cilia provides a way for microorganisms to evade the viscous constraint on direct approach seen for localized thrust. Thus, we next investigate the approach towards target particles by microorganisms propelled by cilia, which might be viewed as the limit of maximally distributed propulsion.

3.1. *Analytical model for approaching spheres – distributed propulsion*

The swimmer and target particle are assumed to be spheres, but to model the ciliated microorganisms, we use a squirmer model in which cilia are replaced by a progressive waving envelope. The velocity boundary condition on the surface of the sphere can be defined by an infinite series of Legendre functions (Blake 1971), but here we employ simplified boundary conditions, used by many researchers (e.g. Ishikawa *et al.* 2006; Molina, Nakayama & Yamamoto 2013) that neglect radial displacement of the boundary and consider only tangential velocities of the boundary of the squirmer sphere. In spherical coordinates (when the origin of the coordinate system is in the centre of the sphere) the tangential velocity at the surface is

$$u_\theta = B_1 \sin\theta + B_2 \sin(2\theta)/2 + B_3(\sin(\theta) + 5\sin(3\theta))/16, \tag{3.1}$$

while u_r and u_ϕ are both zero. Here we consider only three modes parameterized by B_1, B_2, B_3. The parameter B_1 is associated with a source dipole and determines the swimming velocity of the isolated squirmer given by $U = 2B_1/3$. The parameter B_2 is associated with the stresslet around the swimmer and thus the B_2 mode dominates far-field flow generated by the swimmer (Batchelor 1970; Ishikawa *et al.* 2006). For this reason many past studies have only included the B_1 and B_2 modes ($B_3 = 0$), and we study this case first. However, all modes can have similar magnitude near the sphere (as seen in boundary condition equation (3.1)), and so we also consider cases with non-zero third mode B_3 to examine how changes to the near-field structure of the flow can impact approach. Thus for our studies, we specify the boundary condition using two dimensionless parameters $\gamma_2 = B_2/B_1$ and $\gamma_3 = B_3/B_1$, where the squirmer parameter γ_2 determines whether the swimmer is a pusher ($\gamma_2 < 0$), puller ($\gamma_2 > 0$) or neutral ($\gamma_2 = 0$). We report results in terms of kinematic parameters that do not depend on the scale set by the value of B_1. The flow fields around isolated squirmers are plotted in figure 4 for the pusher and puller types.

We assume that a force-free spherical squirmer with radius r_s is approaching a force-free spherical target particle with radius r_t as shown in figure 5. We find the analytical solution using bispherical coordinate system by extending the approach used in § 2 for boundary conditions given by (3.1). The details of the exact solution are given in appendix C.

https://doi.org/10.1017/jfm.2018.509 Published online by Cambridge University Press

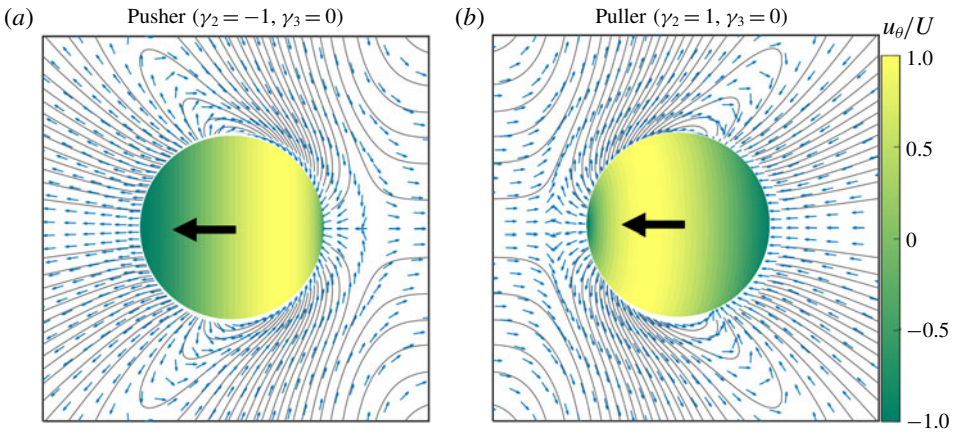


FIGURE 4. (Colour online) The flow field (blue arrows) around and streamlines (grey lines) for different types of spherical squirmers. (*a*) Pushers ($\gamma_2 < 0$) push the flow in the swimming direction during their motions. (*b*) Pullers ($\gamma_2 > 0$) generate flow toward their body against their swimming direction. The colour on the spherical surface shows the tangential velocity component u_θ (3.1) of the surface boundary condition normalized by the swimming velocity U.

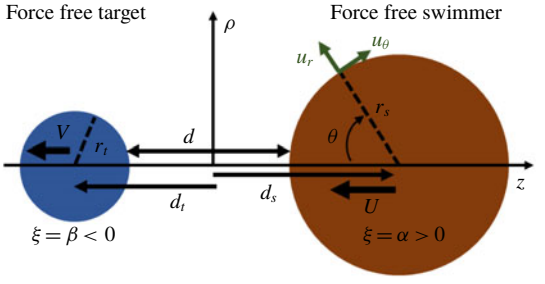


FIGURE 5. (Colour online) The force-free spherical 'squirmer' swimmer (right sphere) with radius r_s approaching a force-free spherical target (left sphere) with radius r_t. For the target sphere, no-slip boundary conditions are imposed. For the squirmer sphere, tangential velocity u_θ is imposed and $u_r = 0$. Note that $\boldsymbol{U} = U\hat{z}$ and $\boldsymbol{V} = V\hat{z}$, but in our calculations $U < 0$ and $V < 0$, so we draw the vectors in the $-\hat{z}$ direction.

In figure 6, we plot the total distance (ΔS) that the swimmer needs to travel before approach to within $0.01r_s$ of the target particle starting from an initial separation of $10r_s$. For comparison we include the results for the swimmer sphere pushed by constant force from figure 3(*b*). In figure 6, The results for the swimmer with only two modes of the surface boundary conditions B_1 and B_2 ($\gamma_3 = 0$) show that for pullers ($\gamma_2 > 0$), the swimmer must travel at most 1.18 (for $r_t/r_s = 0.001$, $\gamma_2 = 0$) times the initial separation, and often less than the initial separation for larger γ_2. Therefore, approach by pullers to target particles is feasible no matter the target size. Pushers with $-0.5 \leqslant \gamma_2 < 0$ show similar behaviour. However, pushers with $\gamma_2 \leqslant -1$ must travel more than three times the initial separation distance, with stronger pushers travelling larger distances to approach the target closely. Therefore, in the context of approach, the behaviour of pusher-type squirmers depends on the

https://doi.org/10.1017/jfm.2018.509 Published online by Cambridge University Press

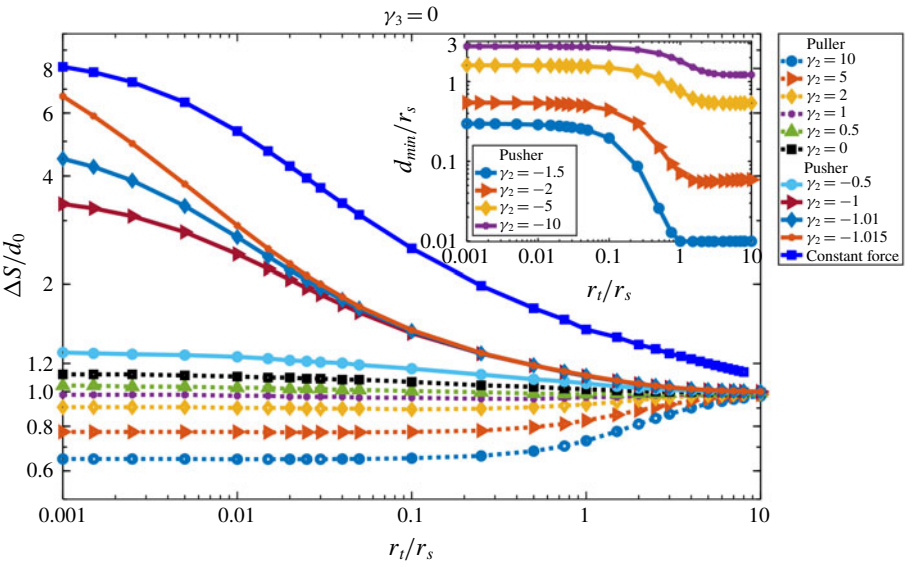


FIGURE 6. (Colour online) Approach to a target by a squirmer with distributed propulsion. Total travelled distance ΔS required for the squirmer to approach within $0.01r_s$ of the target after starting from initial separation $d_0 = 10r_s$, as a function of target : swimmer size ratio r_t/r_s. For comparison, results for the flagellated swimmer are plotted as dark blue diamonds. Pusher-type squirmers ($\gamma_2 < 0$) can approach smaller target particles only when/if the currents that move away from the swimmer (figure 7*a*) are weak ($\gamma_2 > -1$). Puller-type squirmers ($\gamma_2 > 0$) can feasibly approach any size targets due to currents that move toward the swimmer (figure 7*b*). (Inset) Minimum separation d_{min} between the pusher-type squirmer and target. For strong pushers ($\gamma_2 < -1$) the squirmer cannot approach even large targets with $r_t/r_s > 1$.

strength of the squirmer parameter. Weak pushers ($0 > \gamma_2 > -1$) can approach any size target particles, while stronger pusher-type squirmers ($\gamma_2 < -1$) can have difficulty approaching smaller target particles. In fact, as shown in inset of figure 6, for strong enough pushers ($\gamma_2 < -2$) the minimum approach distance d_{min} remains larger than the cutoff $d = 0.01r_s$ even for targets which are larger than the swimmer; hence approach is completely infeasible for strong pushers. In the limit $r_t/r_s \to 0$, the minimum approach distance d_{min} corresponds to the position where the radial velocity field on the centreline ($\theta = 0$) of the isolated swimmer is zero in the swimmer frame, i.e. the stagnation point.

These results for squirmers can be understood in terms of the flow fields generated while swimming. Pullers generate currents that advect particles in front of the swimmer inwards similar to feeding currents. A typical flow field around a puller and target particle is shown in figure 7(*b*). The strength of these currents is controlled by the squirmer parameter (γ_2) and total travelled distances are smaller for the strong currents produced by larger values of γ_2. On the other hand, pushers tend to generate currents that advect particles in front of the swimmer away from the swimmer, hindering approach. A typical flow field for a pusher with $\gamma_2 = -1$ and a target particle is shown in figure 7. Whether or not the current overcomes the swimming translation of the squirmer depends on the magnitude of the (negative) squirmer parameter γ_2.

https://doi.org/10.1017/jfm.2018.509 Published online by Cambridge University Press

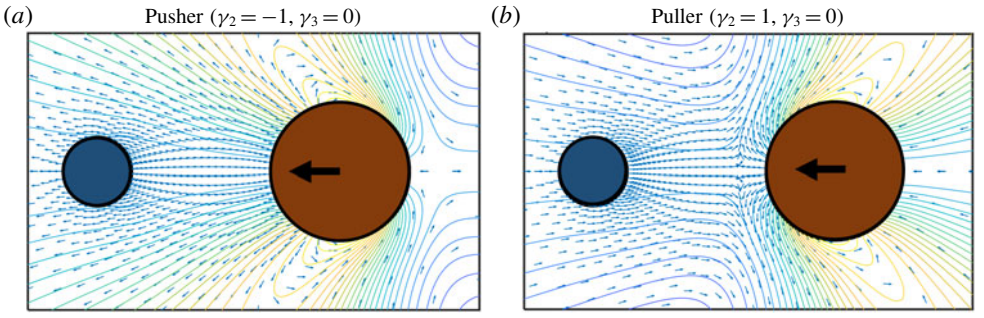


FIGURE 7. (Colour online) Typical flow fields (blue arrows) and streamlines (coloured lines) around a squirmer interacting with a target sphere. (*a*) A pusher ($\gamma_2 < 0$) generates a current that moves the target away from the swimmer, hindering the approach process, while (*b*) a puller generates a current that moves the target toward the swimmer, helping the approach process. The strength of the current for both cases depends on the value of the squirmer parameter (γ_2).

While the B_3 mode decays spatially more quickly compared to the B_2 mode, it can still be important when the surfaces of the swimmer and target are close. We investigate the effect of the B_3 mode on approach to understand how approach is affected by details of the swimming stroke through the near-field flow. In figure 8, we plot the distance ΔS required by the swimmer to approach to the different sizes of the target particles considering B_3 mode. This mode can greatly affect approach dynamics. For $\gamma_3 = 1$, only pullers ($\gamma_2 \geqslant 0$) can approach any sizes of targets while approach for pushers is feasible only for larger targets (figure 8*a*). For $\gamma_3 = -1$, approach for pullers is feasible and only weak pushers with $0 < \gamma_2 \leqslant -5$ can approach to any target sizes (figure 8*b*). In general, B_3 mode with $\gamma_3 > 0$ hinders the feasibility of approach for both pushers and pullers, while $\gamma_3 < 0$ helps them to approach targets. We can find a value for γ_3 such that the approach is feasible for any kind of pusher or puller ($\gamma_3 = -20$, figure 8*c*) or approach is totally infeasible throughout the range of squirming parameters investigated ($\gamma_3 = 20$, figure 8*d*).

These results show that while the B_3 mode spatially decays faster than B_2 mode, by affecting the near-field flow, it can strongly affect the feasibility of approach. Typical flow fields around the swimmer and a target sphere are shown in figure 9 for different strengths of B_3 mode. Comparing the flow field around the swimmer and a target sphere with (figure 7) and without (figure 9) B_3 mode show that pushers ($\gamma_2 < 0$) with smaller values of $\gamma_3 < 0$ can generate flow fields toward the swimmer (like pullers) which helps in approaching targets. On the other hand, pullers ($\gamma_2 > 0$) with bigger values of $\gamma_3 > 0$ generate currents around the swimmer which move the target away from the swimmer like pushers without B_3 mode.

4. Discussion

We have studied the approach of spheres to understand the viscous constraints on the approach of microorganisms to target particles. The swimmer starts at a separation of 10 swimmer radii ($d_0 = 10r_s$) from the target. As a metric, we calculated the total distance travelled by the swimmer until it approaches within a hundredth of the swimmer radius of the target ($d = 0.01r_s$). We use this finite cutoff due to the no-collision paradox, since in many situations actual physical contact would require

https://doi.org/10.1017/jfm.2018.509 Published online by Cambridge University Press

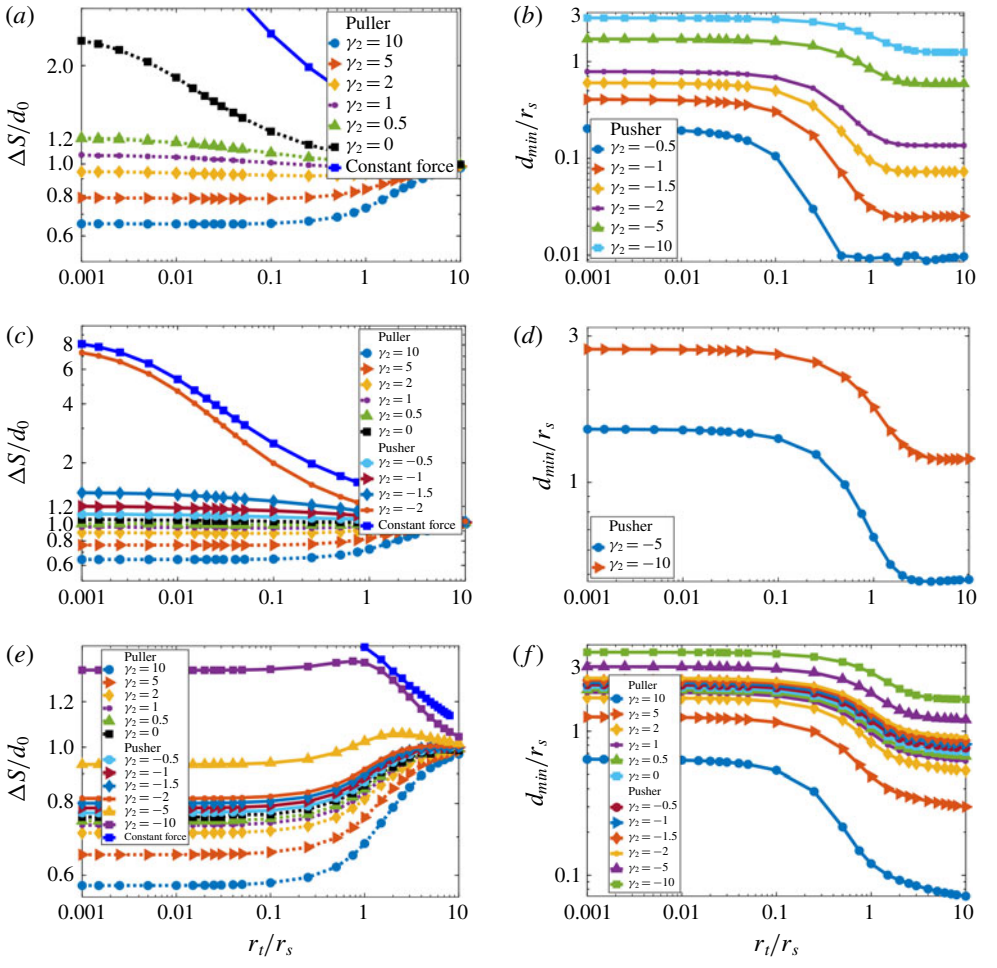


FIGURE 8. (Colour online) Approach to a target by a squirmer with distributed propulsion can be greatly affected by the B_3 mode. (*a*) $\gamma_3 = 1$. Total travelled distance ΔS required for the squirmer to approach different sizes of targets. Puller-type squirmers ($\gamma_2 > 0$) can approach any size of target particles. (*b*) $\gamma_3 = 1$. For pushers targets are only approached to a minimum distance d_{min} which is usually larger than the cutoff distance, hence approach is infeasible. (*c*) $\gamma_3 = -1$. Total travelled distance ΔS required for the squirmer to approach different sizes of targets. Only squirmers with $\gamma_2 > -5$ can approach any size targets. (*d*) $\gamma_3 = -1$. For strong enough pushers ($\gamma_2 < -5$) targets can only be approached to a minimum distance d_{min} larger than the cutoff distance. (*e*,*f*) We can specify values for γ_3 such that approach to targets is always feasible (*e*, $\gamma_3 = -20$, showing distance travelled to approach ΔS) or infeasible (*f*, $\gamma_3 = 20$, showing minimum approach distance d_{min}).

infinite time, and we expect that at small distances physics outside of continuum hydrodynamics would take over between swimmer and target. For example, diffusion via Brownian motion could allow contact between particles. To estimate when such diffusion becomes as important as hydrodynamic approach, consider the timescales needed for a target particle to diffuse by the cutoff distance, $t_{diff} = d^2/(2D)$, where $D = 2k_BT/(6\pi\kappa r_t)$ is the diffusion constant. If t_{diff} is shorter than the advective

https://doi.org/10.1017/jfm.2018.509 Published online by Cambridge University Press

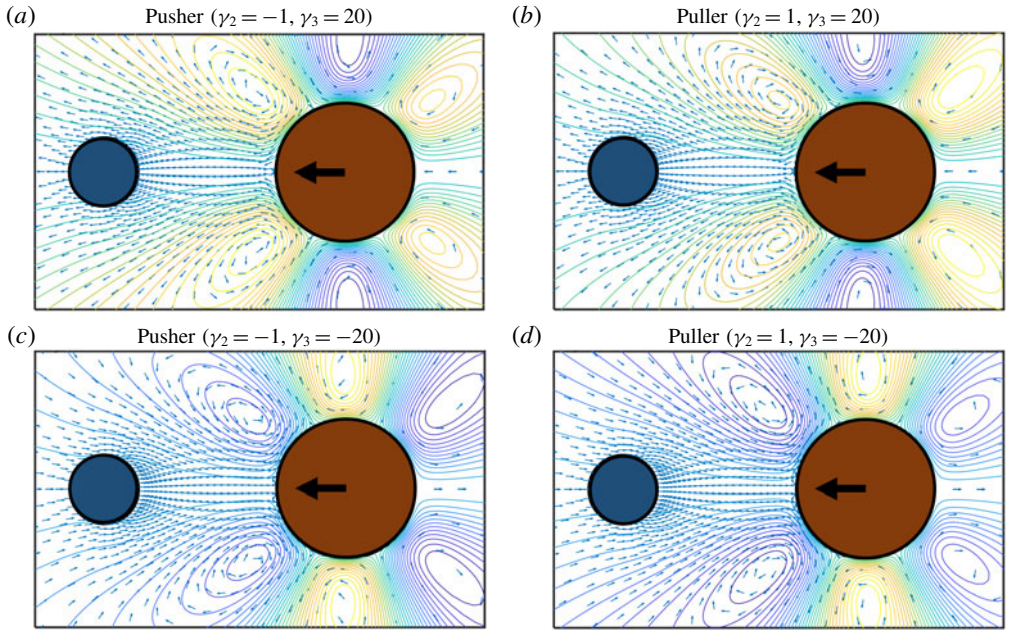


FIGURE 9. (Colour online) Typical flow fields (blue arrows) and streamlines (coloured lines) around a squirmer interacting with a target sphere considering mode B_3. (*a*,*c*) A pusher ($\gamma_2 < 0$) with strong B_3 mode can be act as a stronger pusher $\gamma_3 = 20$ or behaves like a puller $\gamma_3 = -20$, while (*b*,*d*) the effects of the B_3 mode are opposite for a puller. Strength and direction of the generated current around the swimmer depends on the strength of the different modes.

timescale $t_{adv} = d/V$, where V is a typical swimming velocity, then diffusion will be more important than hydrodynamics. For a marine bacterium ($r_s \approx 1$ μm, $V \approx 100$ μm s^{-1}) and at our cutoff distance ($d = 0.01r_s$), $t_{diff}/t_{adv} \approx 4(r_t/r_s)$, so diffusion becomes important for target particles less than about 250 nm in size. For smaller particles, one should only apply our viscous constraints on approach to a larger cutoff distance. Similar estimates for a typical ciliate ($r_s \approx 100$ μm, $V \approx 1000$ μm s^{-1}) or a copepod appendage ($r_s \approx 10$ μm, $V \approx 10$ mm s^{-1} (Koehl & Strickier 1981)) find that $t_{diff}/t_{adv} \approx 20\,000(r_t/r_s)$, so hydrodynamic effects dominate for even smaller targets. However, it should be noted that our criterion underestimates the importance of diffusion since it does not take into account the fact that at such small separations, $t_{adv} = d/V$ is a severe underestimate of approach times precisely because of the viscous effects described in this paper.

First, we modified the exact solution for two spheres with no-slip boundary conditions in bispherical coordinates obtained by Stimson & Jeffery (1926) to investigate a 'swimmer' sphere pushed by constant force towards a target sphere. We found that hydrodynamic constraints prevent the approach of swimmers to smaller target particles, but allow approach to similar- and larger-sized targets. Qualitatively similar results were obtained for a more realistic numerical model of a force-free spherical cell pushed by a rotating flagellum. The similarity between these results arises from the fact that in both cases the propulsion is localized.

These hydrodynamic constraints on approach can be evaded by microorganisms using distributed modes of propulsion. To demonstrate this, we investigated the

https://doi.org/10.1017/jfm.2018.509 Published online by Cambridge University Press

maximally distributed propulsion of squirmer-type swimmers. For a spherical squirmer approaching a spherical target, analytic results for approach can be obtained using bispherical coordinates. The results show that for these models, the feasibility of approach depends on the near-field flows around the swimmer. For squirmers with only the first two modes of tangential surface velocity, we find that puller-type squirmers generate feeding currents that pull particles towards the swimmer, and make approach to any size target particle feasible. On the other hand, strong enough pusher-type squirmers can only approach similar- or larger-sized targets. In general, however, the near-field flows can be controlled by details of the swimmer stroke lying beyond the pusher/puller categorization. In our model, we showed that adding a third mode can make it feasible for pushers, and infeasible for pullers, to approach smaller targets. Thus, unlike swimmers with localized propulsion, swimmers with distributed propulsion (including multiple appendages) have the ability to control approach feasibility.

Our results are broadly consistent with biological observations. Feasibility of the direct approach for a bigger or similar sizes of the target particles even for localized propulsion is demonstrated by bacterial conjugation, mating, fertilization of an egg by sperm. On the other hand, direct approach to smaller prey particles by localized propulsion is difficult, and in these cases microorganisms use other strategies to capturing small food particles. Our squirmer results indicate the importance of feeding currents for prey capture, and point out that feeding currents can be generated by propulsive strokes as well as via non-locomotory behaviour. In addition to feeding currents, our results also shed light on the use of appendages or filters to manipulate or capture smaller target particles (Riisgård & Larsen 2010). An appendage or filtration element could be viewed as an object pushed by an external force (exerted by the rest of the organism) towards a target; thus manipulation or filtration can be successful only if the appendage or filtration element is similar in size or smaller than the target particles.

Our models were limited to relatively simple spherical geometries and head-on approach. Future work could address issues arising from relaxing these conditions. Even though some organisms are quite close to spherical ciliated organisms (Ishikawa *et al.* 2006), there are many organisms with non-spherical ciliated geometries. For instance, *Opalina* and *Paramecium* are more likely to be ellipsoidal than spherical (Lauga & Powers 2009) and employing an ellipsoidal squirmer model can describe their behaviour more appropriately (Theers *et al.* 2016). Distributed propulsion is not restricted to ciliates. Organisms such as copepods can use multiple appendages to generate propulsion as well as currents to pull and manipulate small particles (Kiørboe *et al.* 2014). While the zero Reynolds number assumption of the presented work can approximate manipulation of particles by copepod appendages, inertial effects which are not included in this study may need to be incorporated for direct interaction of copepod bodies and target particles (Li *et al.* 2016).

Although the calculations presented here apply only to direct approach along the centrelines of the spheres, numerical analyses similar to ours could be suitable for studying approach and interactions with more complicated geometries or from different directions, including rotational motions (Ishimoto, Cosson & Gaffney 2016). Trapping dynamics (Spagnolie *et al.* 2015; Desai, Shaik & Ardekani 2018) may become important for these geometries. Finally, understanding the hydrodynamics of near-contact interactions with swimmers is also important for understanding the enhanced diffusion of particles in suspensions of active swimmers (Jeanneret *et al.* 2016) which can depend on close approach.

https://doi.org/10.1017/jfm.2018.509 Published online by Cambridge University Press

Acknowledgement

This work was supported by National Science Foundation grant CBET-CAREER-1651031 to H.C.F.

Appendix A. Analytical model for approaching spheres – localized propulsion

For Stokes flow, the flow velocity field can be described as the curl of a vectorial streamfunction $\boldsymbol{\psi}$ that satisfies the biharmonic equation, $\nabla^4\boldsymbol{\psi} = 0$. For a flow axisymmetric in the angular coordinate ϕ (corresponding to rotation angle about the z axis, figure 1*a*), $\boldsymbol{\psi}$ can be expressed in terms of a scalar ψ, as $\boldsymbol{\psi} = \psi \boldsymbol{e}_\phi$, and the components of the velocity field in the cylindrical coordinate system are

$$u_\rho = \frac{1}{\rho}\frac{\partial \psi}{\partial z}, \tag{A 1a}$$

$$u_z = -\frac{1}{\rho}\frac{\partial \psi}{\partial \rho}. \tag{A 1b}$$

For two interacting spheres, it is convenient to use the bispherical coordinate system (ξ, η, ϕ) (figure 1*a*), for which the general solution was given by Stimson & Jeffery (1926) as

$$\psi = (\cosh\xi - \mu)^{-3/2} X, \tag{A 2a}$$

$$X = \sum_{n=1}^{\infty} U_n(\xi) V_n(\mu), \tag{A 2b}$$

$$\begin{aligned} U_n(\xi) = {} & \mathcal{A}_n \cosh((n-1/2)\xi) + \mathcal{B}_n \sinh((n-1/2)\xi) \\ & + \mathcal{C}_n \cosh((n+3/2)\xi) + \mathcal{D}_n \sinh((n+3/2)\xi), \end{aligned} \tag{A 2c}$$

where $\mu = \cos\eta$ and $\mathcal{A}_n$, $\mathcal{B}_n$, $\mathcal{C}_n$, and $\mathcal{D}_n$ are real constants determined by boundary conditions. The notation $V_n(\mu) = P_{n-1}(\mu) - P_{n+1}(\mu)$ is used for combinations of Legendre functions $P_n(\mu)$ that satisfy the differential equation

$$(1-\mu^2)\frac{\mathrm{d}^2 V_n}{\mathrm{d}\mu^2} + n(n+1)V_n = 0. \tag{A 3}$$

The relations between the cylindrical coordinates (ρ, z, ϕ) and bispherical coordinates (ξ, η, ϕ) are (figure 1*a*),

$$\rho = \frac{c\sin\eta}{\cosh(\xi) - \mu}, \quad z = \frac{c\sinh\xi}{\cosh(\xi) - \mu}, \tag{A 4a,b}$$

where c is a real positive constant and surfaces of constant ξ are non-intersecting spheres centred at $z = c\coth\xi$ with radius $a = c|\mathrm{csch}\,\xi|$. We assume that the swimmer with $\xi = \alpha > 0$ and radius r_s is approaching the target particle with $\xi = \beta < 0$ and radius r_t as shown in figure 1(*b*). Using the above, consider two spheres centred at $d_s = c\coth\alpha$ and $d_t = c\coth\beta$ with surfaces defined by $(z - d_u)^2 + \rho^2 = r_u^2$ with $u \in \{s, t\}$ in cylindrical coordinates. If the sphere surfaces are separated by d, then

$$r_s = c\,\mathrm{csch}\,\alpha, \quad r_t = -c\,\mathrm{csch}\,\beta, \quad d = c(\coth\alpha - \coth\beta) - (r_s + r_t). \tag{A 5a–c}$$

https://doi.org/10.1017/jfm.2018.509 Published online by Cambridge University Press

Defining the target : swimmer size ratio by $r = r_t/r_s$ and $x = 1 + d/r_s$, equations (A 5) can be solved for α, β and c,

$$\alpha = \cosh^{-1}\left(\frac{(x+r)^2 - (r^2-1)}{2(x+r)}\right), \tag{A 6a}$$

$$\beta = -\cosh^{-1}\left(\left|\frac{(x+r)^2 + (r^2-1)}{2r(x+r)}\right|\right), \tag{A 6b}$$

$$\frac{c}{r_s} = \sqrt{\left(\frac{(x+r)^2 - (r^2-1)}{2(x+r)}\right)^2 - 1}. \tag{A 6c}$$

Stimson and Jeffery studied the translation of two spheres moving along their common centreline with the same velocity. Here, we present analogous results for two spheres translating along their common diameter (in the z-direction) with arbitrary velocities V_s and V_t for the swimmer and target, respectively. In cylindrical coordinates, the no-slip boundary conditions at the surface of the spheres are

$$\frac{\partial \psi}{\partial z} = 0, \quad \frac{\partial \psi}{\partial \rho} = -\rho V_s \tag{A 7a,b}$$

on the swimmer, and

$$\frac{\partial \psi}{\partial z} = 0, \quad \frac{\partial \psi}{\partial \rho} = -\rho V_t \tag{A 8a,b}$$

on the target. These boundary conditions can be rewritten in the bispherical coordinate system as (Stimson & Jeffery 1926)

$$\psi + \frac{1}{2}\rho^2 V_s = 0, \quad \frac{\partial}{\partial \xi}\left(\psi + \frac{1}{2}\rho^2 V_s\right) = 0 \tag{A 9a,b}$$

on the swimmer, and

$$\psi + \frac{1}{2}\rho^2 V_t = 0, \quad \frac{\partial}{\partial \xi}\left(\psi + \frac{1}{2}\rho^2 V_t\right) = 0 \tag{A 10a,b}$$

on the target. Using these four equations (A 9) and A 10) for the boundary conditions at the surface of the spheres ($\xi = \alpha$ and $\xi = \beta$) and evaluating the streamfunction (A 2) at the surface of spheres one can determine the unknown coefficients $\mathcal{A}_n$, $\mathcal{B}_n$, $\mathcal{C}_n$, $\mathcal{D}_n$ for each n by solving the system of linear equations

$$\begin{aligned}
&\mathcal{A}_n \cosh(n-\tfrac{1}{2})\alpha + \mathcal{B}_n \sinh(n-\tfrac{1}{2})\alpha + \mathcal{C}_n \cosh(n+\tfrac{3}{2})\alpha + \mathcal{D}_n \sinh(n+\tfrac{3}{2})\alpha \\
&\quad = -kV_s[(2n+3)\mathrm{e}^{-(n-1/2)\alpha} - (2n-1)\mathrm{e}^{-(n+3/2)\alpha}] \qquad \text{(A 11a)} \\
&(2n-1)[\mathcal{A}_n \sinh(n-\tfrac{1}{2})\alpha + \mathcal{B}_n \cosh(n-\tfrac{1}{2})\alpha] \\
&\quad + (2n+3)[\mathcal{C}_n \sinh(n+\tfrac{3}{2})\alpha + \mathcal{D}_n \cosh(n+\tfrac{3}{2})\alpha] \\
&\quad = -kV_s(2n-1)(2n+3)[\mathrm{e}^{-(n-1/2)\alpha} - \mathrm{e}^{-(n+3/2)\alpha}] \qquad \text{(A 11b)} \\
&\mathcal{A}_n \cosh(n-\tfrac{1}{2})\beta + \mathcal{B}_n \sinh(n-\tfrac{1}{2})\beta + \mathcal{C}_n \cosh(n+\tfrac{3}{2})\beta + \mathcal{D}_n \sinh(n+\tfrac{3}{2})\beta \\
&\quad = -kV_t[(2n+3)\mathrm{e}^{(n-1/2)\beta} - (2n-1)\mathrm{e}^{(n+3/2)\beta}] \qquad \text{(A 11c)}
\end{aligned}$$

https://doi.org/10.1017/jfm.2018.509 Published online by Cambridge University Press

$$(2n-1)[\mathcal{A}_n \sinh(n-\tfrac{1}{2})\beta + \mathcal{B}_n \cosh(n-\tfrac{1}{2})\beta] + (2n+3)[\mathcal{C}_n \sinh(n+\tfrac{3}{2})\beta + \mathcal{D}_n \cosh(n+\tfrac{3}{2})\beta] = -kV_t(2n-1)(2n+3)[\mathrm{e}^{(n-1/2)\beta} - \mathrm{e}^{(n+3/2)\beta}], \tag{A 11d}$$

where

$$k = \frac{c^2 n(n+1)}{\sqrt{2}(2n-1)(2n+1)(2n+3)}. \tag{A 12}$$

Forces on the swimmer (F_s) and target particle (F_t) are determined by integrating the stress tensor over the surface of the spheres which, as shown by Stimson & Jeffery (1926), results in

$$F_s = -\kappa \frac{2\pi\sqrt{2}}{c} \sum_{n=1}^{\infty} (2n+1)(\mathcal{A}_n + \mathcal{B}_n + \mathcal{C}_n + \mathcal{D}_n) \tag{A 13a}$$

$$F_t = -\kappa \frac{2\pi\sqrt{2}}{c} \sum_{n=1}^{\infty} (2n+1)(\mathcal{A}_n - \mathcal{B}_n + \mathcal{C}_n - \mathcal{D}_n), \tag{A 13b}$$

where κ is the viscosity of the fluid.

Coefficients $\mathcal{A}_n$, $\mathcal{B}_n$, $\mathcal{C}_n$ and $\mathcal{D}_n$ are linear in the velocities V_s and V_t in (A 11). Therefore, we can find a 2×2 resistance matrix ($\boldsymbol{R}$) that relates forces on the swimmer and target spheres to their velocities, $[F_s; F_t] = \boldsymbol{R}[V_s; V_t]$.

Coefficients $\mathcal{A}_n$, $\mathcal{B}_n$, $\mathcal{C}_n$ and $\mathcal{D}_n$ decay exponentially in α and β and the sums in (A 13) converge rapidly for large separations. However, as the separation decreases more terms are required (Cox & Brenner 1967) to achieve accurate results. For our numerical evaluations we continue to calculate terms until the last term is less than 10^{-15} of the sums for the forces.

Appendix B. Numerical model for flagellated microswimmers

We assume a rigid helical flagellar filament with filament radius a_f, helical radius R_f, and helical pitch P_f (numerical values in table 1), oriented in the z-direction. The centreline of the flagellar filament is a helix with a taper such that it smoothly attaches to the hook (Ramia *et al.* 1993; Hyon *et al.* 2012) given by

$$\boldsymbol{r}_c(z) = R_f(1 - \mathrm{e}^{-(2\pi z/P_f)^2})[\cos(2\pi z/P_f)\hat{\boldsymbol{x}} + \sin(2\pi z/P_f)\hat{\boldsymbol{y}}] + z\hat{\boldsymbol{z}}. \tag{B 1}$$

The Stokes flow field external to the surface of the cell body, target particle and flagellar filament is expressed in integral form by

$$\boldsymbol{u}(\boldsymbol{x}) = \sum_{m=\{c,t\}} \int_{A_m} \boldsymbol{S}(\boldsymbol{x}-\boldsymbol{x}') \cdot \boldsymbol{q}(\boldsymbol{x}')\, \mathrm{d}A_m(\boldsymbol{x}') - \sum_{m=\{c,t\}} \int_{A_m} \boldsymbol{H}(\boldsymbol{x}-\boldsymbol{x}') \cdot \boldsymbol{u}(\boldsymbol{x}')\, \mathrm{d}A_m(\boldsymbol{x}') + \int_{C_f} [\boldsymbol{S}(\boldsymbol{x}-\boldsymbol{x}')\boldsymbol{f}_f - a_f^2 \boldsymbol{D}(\boldsymbol{x}-\boldsymbol{x}')(\boldsymbol{I}-\boldsymbol{tt}) \cdot \boldsymbol{f}_f]\, \mathrm{d}x'. \tag{B 2}$$

Indices c, t and f stand for the cell body, target sphere and flagellar filament respectively. The first two terms on the right-hand side of (B 2) are BEM contributions to the velocity from the surfaces of the cell body (A_c) and target (A_t) spheres, where $\boldsymbol{u}$ and $\boldsymbol{q}$ are the velocity field and traction force of the flow, respectively,

https://doi.org/10.1017/jfm.2018.509 Published online by Cambridge University Press

Flagellar filament				Cell body
Flagellar pitch	Filament radius	Helical radius	Axial length	Radius
P_f (μm)	a_f (μm)	R_f (μm)	L_f (μm)	r_s (μm)
1.58	0.035	0.14	2.97	1

TABLE 1. Dimensions of the cell body and flagellar filament used for numerical simulations (Constantino *et al.* 2016).

$\boldsymbol{S}(\boldsymbol{x}-\boldsymbol{x}') = (1/8\pi\kappa)(\boldsymbol{I}/|\boldsymbol{x}-\boldsymbol{x}'| + (\boldsymbol{x}-\boldsymbol{x}')(\boldsymbol{x}-\boldsymbol{x}')/|\boldsymbol{x}-\boldsymbol{x}'|^3)$ is the Oseen tensor for a Stokeslet flow, and $\boldsymbol{H}(\boldsymbol{x}-\boldsymbol{x}') = (-3/4\pi\kappa)((\boldsymbol{x}-\boldsymbol{x}')(\boldsymbol{x}-\boldsymbol{x}')/|\boldsymbol{x}-\boldsymbol{x}'|^5)(\boldsymbol{x}-\boldsymbol{x}')\cdot\boldsymbol{n}$ is its associated traction field for a surface with unit outward normal $\boldsymbol{n}$. $\boldsymbol{I}$ is the identity matrix. The last term on the right-hand side of (B 2) is the SBT contribution to the flow coming from the centreline of the flagellar filament C_f with filament radius a_f, where $\boldsymbol{D}$ is the Stokeslet dipole, $\boldsymbol{f}_f$ is the force distribution on C_f and $(\boldsymbol{I}-\boldsymbol{tt})\cdot\boldsymbol{f}_f$ is the component of the force perpendicular to the tangent of the centreline $\boldsymbol{t}$.

The total forces $\boldsymbol{F}_m$ and torques $\boldsymbol{T}_m$ on the cell body and target sphere ($m = \{c, t\}$), and the total force $\boldsymbol{F}_f$ and torque $\boldsymbol{T}_f$ on the flagellar filament are

$$\boldsymbol{F}_m = \int_{A_m} \boldsymbol{q}(\boldsymbol{x})\,\mathrm{d}A_m, \quad \boldsymbol{T}_m = \int_{A_m} (\boldsymbol{x}-\boldsymbol{x}_m)\times\boldsymbol{q}(\boldsymbol{x})\,\mathrm{d}A_m, \quad m\in\{c,t\} \tag{B 3a,b}$$

$$\boldsymbol{F}_f = \int_{C_f} \boldsymbol{f}_f(\boldsymbol{x})\,\mathrm{d}x', \quad \boldsymbol{T}_f = \int_{C_f} (\boldsymbol{x}-\boldsymbol{x}_c)\times\boldsymbol{f}_f(\boldsymbol{x})\,\mathrm{d}x'. \tag{B 3c,d}$$

The boundary conditions are given by

$$\boldsymbol{u}(\boldsymbol{x}) = \boldsymbol{V}_m + \boldsymbol{\Omega}_m\times(\boldsymbol{x}-\boldsymbol{x}_m), \quad \forall\boldsymbol{x}\in A_m,\ m\in\{c,t\} \tag{B 4a}$$

$$\boldsymbol{u}(\boldsymbol{x}) = \boldsymbol{V}_c + (\boldsymbol{\Omega}_c+\boldsymbol{\omega}_f)\times(\boldsymbol{x}-\boldsymbol{x}_c), \quad \forall\boldsymbol{x}\in C_f, \tag{B 4b}$$

where $\boldsymbol{V}_m$ and $\boldsymbol{\Omega}_m$ are the translational and rotational velocities of the cell body or target sphere identified by index m, $\boldsymbol{\omega}_f$ is the relative rotational velocities of the flagellar filament with respect to the cell body and $\boldsymbol{x}_m$ are the centres of the cell body or target sphere.

To evaluate the first two terms of the right-hand side of (B 2), we discretize the surface of the cell body and target sphere into M_c and M_t, respectively, distinct triangular surface elements. Assuming a constant traction $\boldsymbol{q}$ or velocity $\boldsymbol{u}$ on each element, the integrals in (B 2) are numerically evaluated using 27 Gaussian quadrature points (Dunavant 1985) for non-singular elements. We use an analytical approach to remove the singularity in the integrand of (B 2) when points $\boldsymbol{x}$ and $\boldsymbol{x}'$ are on the same triangular element, by subdividing into triangular elements for which $\boldsymbol{x}'$ is on vertex of subelements (Pozrikidis 2002). To evaluate the last term in (B 2), we discretize the slender flagellar filament into M_f straight rods of length δs and assume constant force $\boldsymbol{f}_f$ over each segment (Higdon 1979). For one segment, the result of the integral can be evaluated analytically (see equation 13 of Higdon (1979)).

We evaluate (B 2) at collocation points at the centroid of areal elements or segments, so that there are a total of $(M_c + M_t + M_f)$ collocation points. The result is a $3(M_c + M_t + M_f)$ system of linear algebraic equations written in matrix form as

$$\begin{bmatrix} I_{cc}+H_{cc} & 0_{cf} & H_{ct} \\ H_{fc} & I_{ff} & H_{ft} \\ H_{tc} & 0_{tf} & I_{tt}+H_{tt} \end{bmatrix} \begin{Bmatrix} \boldsymbol{u}_c \\ \boldsymbol{u}_f \\ \boldsymbol{u}_t \end{Bmatrix} = \begin{bmatrix} S_{cc} & K_{cf} & S_{ct} \\ S_{fc} & K_{ff} & S_{ft} \\ S_{tc} & K_{tf} & S_{tt} \end{bmatrix} \begin{Bmatrix} \boldsymbol{f}_c \\ \boldsymbol{f}_f \\ \boldsymbol{f}_t \end{Bmatrix}, \tag{B 5}$$

https://doi.org/10.1017/jfm.2018.509 Published online by Cambridge University Press

where $\boldsymbol{I}$, $\boldsymbol{0}$ are identity and zero matrices. Here we use a compact notation such that (for example) $\boldsymbol{u}_c$ and $\boldsymbol{f}_c$ are $3M_c$-vectors containing all three components of the velocity or force at each of the M_c collocation points on the cell body. The matrices S_{mn} $(m = \{t, c, f\}, n = \{t, c\})$ are each a $M_m \times M_n$ block matrix of 3×3 submatrices; where each submatrix comes from the evaluation of the integral $(1/A)\int_A \boldsymbol{S}(\boldsymbol{x}-\boldsymbol{x}')\,\mathrm{d}A(\boldsymbol{x}')$ contributing to the velocity at a collocation point on sphere or filament m due to an element on sphere or filament n with area A. The matrices H_{mn} $(m = \{t, c, f\}, n = \{t, c\})$ are each a $M_m \times M_n$ block matrix of 3×3 submatrices; where each submatrix comes from the evaluation of the integral $(1/A)\int_A \boldsymbol{H}(\boldsymbol{x}-\boldsymbol{x}')\,\mathrm{d}A(\boldsymbol{x}')$ contributing to the velocity at a collocation point on sphere or filament m due to an element on sphere n with area A. The matrices K_{mf} $(m = \{t, c, f\})$ are each a $M_m \times M_f$ block matrix of 3×3 submatrices; where each submatrix comes from the evaluation of the integral $(1/\delta s)\int_{\delta s} \boldsymbol{S}(\boldsymbol{x}-\boldsymbol{x}') - a_f^2\boldsymbol{D}(\boldsymbol{x}-\boldsymbol{x})(\boldsymbol{I}-\boldsymbol{tt})\,\mathrm{d}A(\boldsymbol{x}')$ contributing to the velocity at a collocation point on sphere or filament m due to a segment of the filament n with length δs.

We consider a force-free swimmer with prescribed relative rotation rate for the flagellum ($\boldsymbol{\omega}_f$) approaching a force-free target sphere. Thus, the force and torque conditions of the swimmer and target particle are

$$\boldsymbol{F}_c + \boldsymbol{F}_f = 0, \quad \boldsymbol{T}_c + \boldsymbol{T}_f = 0, \quad \boldsymbol{F}_t = 0, \quad \boldsymbol{T}_t = 0. \tag{B 6a–d}$$

The velocity boundary conditions (B 4) and force conditions (B 6) can also be written in matrix form (Martindale, Jabbarzadeh & Fu 2016),

$$\begin{Bmatrix} \boldsymbol{u}_c \\ \boldsymbol{u}_f \\ \boldsymbol{u}_t \end{Bmatrix} = \boldsymbol{L} \begin{Bmatrix} \boldsymbol{V}_c \\ \boldsymbol{\Omega}_c \\ \boldsymbol{V}_t \\ \boldsymbol{\Omega}_t \end{Bmatrix} + \begin{Bmatrix} \boldsymbol{0} \\ \boldsymbol{\omega}_f \times (\boldsymbol{x}-\boldsymbol{x}_c) \\ \boldsymbol{0} \end{Bmatrix}, \tag{B 7a}$$

$$\begin{Bmatrix} \boldsymbol{F}_c \\ \boldsymbol{T}_c \\ \boldsymbol{F}_t \\ \boldsymbol{T}_t \end{Bmatrix} = \boldsymbol{L}^T \begin{Bmatrix} \boldsymbol{f}_c \\ \boldsymbol{f}_f \\ \boldsymbol{f}_t \end{Bmatrix}, \tag{B 7b}$$

where $\boldsymbol{L}$ is a $6 \times 3(M_c + M_f + M_t)$ matrix as described in Martindale *et al.* (2016) which allows us to represent the velocity at the collocation points on the surfaces in terms of the translational and rotational velocities. In the last term of (B 7*a*), $\boldsymbol{\omega}_f \times (\boldsymbol{x}-\boldsymbol{x}_c)$ is the prescribed rotation of collocation points on the flagellum.

The force and torque conditions (B 6) give 12 equations to be solved for 12 unknown components of the translational and rotational velocities ($\boldsymbol{V}_c$, $\boldsymbol{\Omega}_c$, $\boldsymbol{V}_t$, $\boldsymbol{\Omega}_t$) in (B 7). To allow direct comparison with the analytical model, at each time step the prescribed rotation rate is adjusted so that the magnitude of $\boldsymbol{F}_f$ is equal to the propulsion force F in § 2. Note that we characterize the approach of a swimmer to targets using the kinematic parameter ΔS, which is independent of choice of force F or rotation rate of the flagellum. Integrating these velocities using a fourth-order Runge–Kutta method yields trajectories of the swimmer and target particle.

The accuracy of the SBT depends on the slenderness parameter and total number of segments on the flagellar filament as described in (Jabbarzadeh, Hyon & Fu 2014; Martindale *et al.* 2016). We discretize the flagellar filament into 140 segments with slenderness parameter $\delta s/a_f = 10$. In addition, we use adaptive discretization for the surface of the cell body and target particle to accurately capture hydrodynamic

https://doi.org/10.1017/jfm.2018.509 Published online by Cambridge University Press

interactions when spheres are close or the size ratio is small (figure 3*a*). For separations $d/r_s > 0.5$, the surface of the swimmer and target sphere is divided into 284 nearly equal-size triangles. When $d/r_s \leqslant 0.5$, the elements near the contact region are refined to smaller triangular elements such that the gap distance is always 5 times greater than the smallest element on the surfaces as shown in figure 3(*a*). The maximum number of surface elements on each sphere used in this study is 3521 for the minimum separation of $d/r_s = 0.01$.

Appendix C. Analytical model for approaching spheres – distributed propulsion

In spherical coordinates (when the origin of the coordinate system is in the centre of the sphere) the tangential velocity at the surface is defined by (3.1) as

$$u_\theta = B_1 \sin\theta + B_2 \sin(2\theta)/2 + B_3(\sin(\theta) + 5\sin(3\theta))/16. \tag{C 1}$$

We assume that a spherical squirmer with radius r_s is approaching a spherical target particle with radius r_t as shown in figure 5. Including translational swimming speed U in the z-direction, velocity boundary conditions for a symmetric spherical squirmer mode in the laboratory frame are (Blake 1971),

$$u_r = U\cos\theta, \tag{C 2a}$$
$$u_\theta = (-U + B_1)\sin\theta + B_2 \sin(2\theta)/2 + B_3(\sin(\theta) + 5\sin(3\theta))/16, \tag{C 2b}$$

where θ is the angle between the swimming direction z and any point on the surface of the sphere in the coordinate system with origin at the squirmer centre (figure 5). These equations can be expressed in cylindrical coordinate system,

$$u_z = u_\theta \sin\theta - u_r \cos\theta, \tag{C 3a}$$
$$u_\rho = u_\theta \cos\theta + u_r \sin\theta, \tag{C 3b}$$

where $\cos\theta = (d_s - z)/r_s$, $\sin\theta = \rho/r_s$ and d_s is distance of the centre of the swimmer sphere from the origin of the cylindrical coordinate system.

We solve this problem in the bispherical coordinate system using the same streamfunction approach as in § 2. Now the coefficients $\mathcal{A}_n$, $\mathcal{B}_n$, $\mathcal{C}_n$ and $\mathcal{D}_n$ in (A 2) are determined by the new boundary conditions described in (C 3). The boundary condition on the swimmer can be expressed in terms of the Stokes stream function in bispherical coordinate using (C 2) and (C 3) as:

$$\frac{\partial\psi}{\partial\xi} = -u_\theta \frac{\rho z r_s}{c}, \quad \frac{\partial\psi}{\partial\eta} = -u_r \frac{\rho z r_s}{c}. \tag{C 4a,b}$$

We can also use (A 2) to obtain derivatives of the streamfunction.

$$\left.\begin{aligned} \frac{\partial\psi}{\partial\xi} &= \left[-\frac{3}{2}\sinh(\xi)X + (\cosh(\xi) - \mu)\frac{\partial X}{\partial\xi}\right](\cosh(\xi) - \mu)^{-5/2}, \\ \frac{\partial\psi}{\partial\eta} &= \left[-\frac{3}{2}X - (\cosh(\xi) - \mu)\frac{\partial X}{\partial\mu}\right]\frac{\rho}{c}(\cosh(\xi) - \mu)^{-3/2}. \end{aligned}\right\} \tag{C 5}$$

Combining (C 4), (C 5) and applying the recurrence relations for Legendre functions,

$$(2n+1)\mu P_n(\mu) = (n+1)P_{n+1}(\mu) + nP_{n-1}(\mu), \tag{C 6a}$$
$$\mu V_n(\mu) = \frac{n-1}{2n-1}V_{n-1}(\mu) + \frac{n+2}{2n+3}V_{n+1}(\mu), \tag{C 6b}$$

https://doi.org/10.1017/jfm.2018.509 Published online by Cambridge University Press

we have

$$\sum_{n=1}^{\infty}\left[\frac{3}{2}\sinh(\alpha)U_n-\cosh(\xi)U_n'+\frac{n}{2n+1}U_{n+1}'+\frac{n+1}{2n+1}U_{n-1}'\right]V_n(\mu)$$
$$=\left[-U+B_1+B_2\left(\frac{\mu\cosh(\alpha)-1}{\cosh(\alpha)-\mu}\right)+B_3\left(\frac{5}{4}\left(\frac{\mu\cosh(\alpha)-1}{\cosh(\alpha)-\mu}\right)^2-\frac{1}{4}\right)\right]$$
$$\times\frac{c^2\sinh(\alpha)(1-\mu^2)}{(\cosh(\alpha)-\mu)^{1/2}},\tag{C 7}$$

$$\sum_{n=1}^{\infty}\left[\left(n+\frac{5}{2}\right)U_{n+1}+\left(n-\frac{3}{2}\right)U_{n-1}-\cosh(\alpha)(2n+1)U_n\right]P_n(\mu)$$
$$=U\left(\frac{\mu\cosh(\alpha)-1}{\cosh(\alpha)-\mu}\right)c^2(\cosh(\alpha)-\mu)^{1/2},\tag{C 8}$$

where $U_n'=\partial U_n/\partial\xi$ and in (C 8)–(C 20), U_n and U_n' are evaluated at $\xi=\alpha$. To solve this, we perform Taylor–Legendre expansions on the right-hand side of (C 8) and (C 9) as

$$\sum_{n=1}^{\infty}E_n(\alpha)V_n(\mu)\equiv\left[-U+B_1+B_2\left(\frac{\mu\cosh(\alpha)-1}{\cosh(\alpha)-\mu}\right)\right.$$
$$\left.+B_3\left(\frac{5}{4}\left(\frac{\mu\cosh(\alpha)-1}{\cosh(\alpha)-\mu}\right)^2-\frac{1}{4}\right)\right]\frac{c^2\sinh(\alpha)(1-\mu^2)}{(\cosh(\alpha)-\mu)^{1/2}},\tag{C 9}$$

$$\sum_{n=0}^{\infty}F_n(\alpha)P_n(\mu)\equiv U\left(\frac{\mu\cosh(\alpha)-1}{\cosh(\alpha)-\mu}\right)c^2(\cosh(\alpha)-\mu)^{1/2}.\tag{C 10}$$

In a Taylor–Legendre expansion, any piecewise smooth function $f(x)$ on $[-1,1]$ can be expressed as a series in $P_n(\xi)$ and $V_n(\xi)$

$$f(x)=\sum_{n=0}^{\infty}a_nP_n(x),\tag{C 11}$$

with a_n determined by

$$a_n=\frac{2n+1}{2}\int_{-1}^{1}f(x)P_n(x)\,\mathrm{d}x.\tag{C 12}$$

Thus, to find E_n and F_n, we must evaluate (C 12) using the following relations

$$\int_{-1}^{+1}\frac{V_n\mathrm{d}\mu}{(\cosh(\xi)-\mu)^{1/2}}=2\sqrt{2}\left[\frac{\mathrm{e}^{-(n-1/2)|\xi|}}{2n-1}-\frac{\mathrm{e}^{-(n+3/2)|\xi|}}{2n+3}\right]\tag{C 13a}$$

$$xf(x)=\sum_{n=0}^{\infty}\left[\frac{n}{2n-1}a_{n-1}+\frac{n+1}{2n+3}a_{n+1}\right]P_n(x)\tag{C 13b}$$

$$(1-x^2)f(x)=\sum_{n=0}^{\infty}\frac{n(n+1)}{2n+1}\left[\frac{a_{n-1}}{2n-1}+\frac{a_{n+1}}{2n+3}\right]V_n(x)\tag{C 13c}$$

https://doi.org/10.1017/jfm.2018.509 Published online by Cambridge University Press

$$x(1-x^2)f(x) = \sum_{n=0}^{\infty} \frac{n(n+1)}{2n+1}\left[\frac{(n-1)a_{n-1}}{(2n-1)(2n-3)} + \frac{a_n}{(2n-1)(2n+3)} - \frac{(n+2)a_{n+2}}{(2n+5)(2n+3)}\right] V_n(x) \quad (C\,13d)$$

$$(1-x^2)P_n(x) = \frac{(n+1)(n+2)}{(2n+1)(2n+3)}V_{n+1} - \frac{n(n-1)}{(2n+1)(2n-1)}V_{n-1}. \quad (C\,13e)$$

Other necessary integrals can be derived from this equation by differentiation with respect to ξ. We find E_n and F_n as,

$$F_n(\alpha) = \sqrt{2}c^2 U(\cosh(\alpha)\left[\frac{n}{2n-1}\mathrm{e}^{-(n-1/2)\alpha} + \frac{n+1}{2n+3}\mathrm{e}^{-(n+3/2)\alpha}\right] - \mathrm{e}^{-(n+1/2)\alpha}) \quad (C\,14)$$

$$E_n(\alpha) = \sqrt{2}c^2(U-B_1)\sinh(\alpha)\frac{n(n+1)}{2n+1}\left(\frac{\mathrm{e}^{-(n-1/2)\alpha}}{2n-1} - \frac{\mathrm{e}^{-(n+3/2)\alpha}}{2n+3}\right) \quad (C\,15)$$

$$+\sqrt{2}c^2B_2\frac{n(n+1)}{2n+1}\left[\cosh(\alpha)\left(\frac{(n-1)\mathrm{e}^{-(n-3/2)\alpha}}{2n-1} + \frac{(2n+1)\mathrm{e}^{-(n+1/2)\alpha}}{(2n+3)(2n-1)} - \frac{(n+2)\mathrm{e}^{-(n-5/2)\alpha}}{2n+3}\right) - \left(\mathrm{e}^{-(n-1/2)\xi} - \mathrm{e}^{-(n+3/2)\alpha}\right)\right]$$

$$+\sqrt{2}c^2B_3\frac{\sinh(\alpha)}{12}\frac{n(n+1)}{2n+1}\left(\frac{5\mathrm{e}^{-(n+5/2)\alpha}(n-1)(n-2)}{(2n-1)}\right. \quad (C\,16)$$

$$+\frac{3\mathrm{e}^{-(n-3/2)\alpha}(10n^3+25n^2+7n-6)}{(2n-1)(2n+3)} \quad (C\,17)$$

$$\left.+\frac{\mathrm{e}^{-(n+1/2)\alpha}(-30n^3-15n^2+39n+6)}{(2n-1)(2n+3)} - \frac{5\mathrm{e}^{-(n+7/2)\alpha}(n+2)(n+3)}{(2n+3)}\right). \quad (C\,18)$$

Equations (C 8) and (C 9) then yield recurrence relations for U_n and U_n',

$$\frac{3}{2}\sinh(\alpha)U_n - \cosh(\alpha)U_n' + \frac{n}{2n+1}U_{n+1}' + \frac{n+1}{2n+1}U_{n-1}' = E_n(\alpha), \quad (C\,19)$$

$$(n+\tfrac{5}{2})U_{n+1} + (n-\tfrac{3}{2})U_{n-1} - \cosh(\alpha)(2n+1)U_n = F_n(\alpha). \quad (C\,20)$$

We calculate $U_n(\xi=\alpha)$ and $U_n'(\xi=\alpha)$ from (C 19) and (C 20), and after some simplification, can write

$$U_n(\xi=\alpha) = -kU\left[(2n+3)\mathrm{e}^{-(n-1/2)\alpha} - (2n-1)\mathrm{e}^{-(n+3/2)\alpha}\right] \quad (C\,21)$$

$$U_n'(\xi=\alpha) = UH_n(\alpha) + G_n(\alpha), \quad (C\,22)$$

where the expressions $H_n(\alpha)$ and $G_n(\alpha)$ can be found from recurrence relation (C 19) but are not illuminating to write down explicitly.

Therefore, (A 11) that determine the coefficients $\mathcal{A}_n$, $\mathcal{B}_n$, $\mathcal{C}_n$, $\mathcal{D}_n$ are altered, with (A 11*a*,*b*) replaced by

$$\mathcal{A}_n\cosh(n-\tfrac{1}{2})\alpha + \mathcal{B}_n\sinh(n-\tfrac{1}{2})\alpha + \mathcal{C}_n\cosh(n+\tfrac{3}{2})\alpha + \mathcal{D}_n\sinh(n+\tfrac{3}{2})\alpha$$
$$= -kU[(2n+3)\mathrm{e}^{-(n-1/2)\alpha} - (2n-1)\mathrm{e}^{-(n+3/2)\alpha}] \quad (C\,23a)$$

https://doi.org/10.1017/jfm.2018.509 Published online by Cambridge University Press

$$(2n-1)[\mathcal{A}_n \sinh(n-\tfrac{1}{2})\alpha + \mathcal{B}_n \cosh(n-\tfrac{1}{2})\alpha] + (2n+3)[\mathcal{C}_n \sinh(n+\tfrac{3}{2})\alpha + \mathcal{D}_n \cosh(n+\tfrac{3}{2})\alpha] = UH_n(\alpha) + G_n(\alpha), \tag{C 23b}$$

while (A 11*c*,*d*) remain unaltered. Equations (C 23) describe the motion of the squirmer with translational swimming speed U, while (A 11*c*,*d*) describe the motion of the target sphere with no-slip boundary conditions on the surface translating with velocity V_t. As before, the force (F_s) on the swimmer ($\xi = \alpha > 0$) and force (F_t) on the target sphere ($\xi = \beta < 0$) can be calculated by (A 13). The swimmer and target sphere are both assumed to be force free ($F_s = 0$ and $F_t = 0$). Given sphere radii r_s and r_t and their separation d, the quantities c, α and β in the bispherical coordinate system are obtained using (A 5). Specification of the problem is completed by the squirmer mode strengths B_1, B_2 and B_3. The parameters γ_2 and γ_3 determine B_2 and B_3, respectively, relative to B_1. With γ_2 and γ_3 fixed, B_1 does not have to be specified since our results for the kinematic parameter ΔS do not depend on B_1.

Equations (C 23*a*,*b*) and (A 11*c*,*d*) are linear in the translational velocities U and V and parameters B_1, B_2 and B_3 for the swimmer and target sphere. Therefore we can relate the forces to the velocities and parameters via

$$\begin{bmatrix} F_s \\ F_t \end{bmatrix} = \boldsymbol{R} \begin{bmatrix} U \\ V_t \end{bmatrix} + \boldsymbol{B} \begin{bmatrix} B_1 \\ B_2 \\ B_3 \end{bmatrix}, \tag{C 24}$$

where $\boldsymbol{R}$ and $\boldsymbol{B}$ are 2×2 and 2×3 matrices that depend on the separation d between spheres (in addition to the sphere sizes). For given mode strengths B_1, B_2 and B_3, we solve (C 24) under the force-free conditions to obtain the translational velocities U and V_t, then integrate them to find the trajectories of the spheres starting from an initial separation d_0.

REFERENCES

ALBERTS, B., JOHNSON, A., LEWIS, J., RAFF, M., ROBERTS, K. & WALTER, P. 2002 *Molecular Biology of the Cell*. Garland Science.

BALAZS, A. C., BHATTACHARYA, A., TRIPATHI, A. & SHUM, H. 2014 Designing bioinspired artificial cilia to regulate particle–surface interactions. *J. Phys. Chem. Lett.* **5** (10), 1691–1700.

BATCHELOR, G. K. 1970 The stress system in a suspension of force-free particles. *J. Fluid Mech.* **41** (3), 545–570.

BLAKE, J. R. 1971 A spherical envelope approach to ciliary propulsion. *J. Fluid Mech.* **46** (1), 199–208.

BRAGA, R. M., DOURADO, M. N. & ARAÚJO, W. L. 2016 Microbial interactions: ecology in a molecular perspective. *Brazilian J. Microbiol.* **47**, 86–98.

BRENNER, H. 1961 The slow motion of a sphere through a viscous fluid towards a plane surface. *Chem. Engng Sci.* **16** (3–4), 242–251.

CONSTANTINO, M. A., JABBARZADEH, M., FU, H. C. & BANSIL, R. 2016 Helical and rod-shaped bacteria swim in helical trajectories with little additional propulsion from helical shape. *Sci. Adv.* **2** (11), e1601661.

COX, R. G. & BRENNER, H. 1967 The slow motion of a sphere through a viscous fluid towards a plane surfaceii small gap widths, including inertial effects. *Chem. Engng Sci.* **22** (12), 1753–1777.

DESAI, N., SHAIK, V. A. & ARDEKANI, A. M. 2018 Hydrodynamics-mediated trapping of micro-swimmers near drops. *Soft Matt.* **14** (2), 264–278.

https://doi.org/10.1017/jfm.2018.509 Published online by Cambridge University Press

DUNAVANT, D. A. 1985 High degree efficient symmetrical Gaussian quadrature rules for the triangle. *Intl J. Numer. Methods Engng* **21** (6), 1129–1148.

GRIFFITHS, A. J. F., MILLER, J. H., SUZUKI, D. T., LEWONTIN, R. C., GELBART, W. M. & OTHERS 2000 Transcription: an overview of gene regulation in eukaryotes. In *An Introduction to Genetic Analysis*, 7th edn. WH Freeman.

GROSSART, H. P., KIØRBOE, T., TANG, K. W., ALLGAIER, M., YAM, E. M. & PLOUG, H. 2006 Interactions between marine snow and heterotrophic bacteria: aggregate formation and microbial dynamics. *Aquatic Microbial Ecol.* **42**, 19–26.

HANSEN, B., BJORNSEN, P. K. & HANSEN, P. J. 1994 The size ratio between planktonic predators and their prey. *Limnol. Oceanogr.* **39** (2), 395–403.

HIGDON, J. J. L. 1979 A hydrodynamic analysis of flagellar propulsion. *J. Fluid Mech.* **90** (4), 685–711.

HYON, Y., POWERS, T. R., STOCKER, R., FU, H. C. & OTHERS 2012 The wiggling trajectories of bacteria. *J. Fluid Mech.* **705**, 58–76.

ISHIKAWA, T., SIMMONDS, M. P. & PEDLEY, T. J. 2006 Hydrodynamic interaction of two swimming model micro-organisms. *J. Fluid Mech.* **568**, 119–160.

ISHIMOTO, K., COSSON, J. & GAFFNEY, E. A. 2016 A simulation study of sperm motility hydrodynamics near fish eggs and spheres. *J. Theor. Biol.* **389**, 187–197.

JABBARZADEH, M., HYON, Y. & FU, H. C. 2014 Swimming fluctuations of micro-organisms due to heterogeneous microstructure. *Phys. Rev.* E **90** (4), 043021.

JEANNERET, R., PUSHKIN, D. O., KANTSLER, V. & POLIN, M. 2016 Entrainment dominates the interaction of microalgae with micron-sized objects. *Nature Commun.* **7**, 12518.

JOHNKE, J., BOENIGK, J., HARMS, H. & CHATZINOTAS, A. 2017 Killing the killer: predation between protists and predatory bacteria. *FEMS Microbiol. Lett.* **364** (9), fnx089.

KIØRBOE, T. 2007 Mate finding, mating, and population dynamics in a planktonic copepod Oithona davisae: there are too few males. *Limnol. Oceanogr.* **52** (4), 1511–1522.

KIØRBOE, T. 2016 Fluid dynamic constraints on resource acquisition in small pelagic organisms. *European Phys. J. Special Topics* **225** (4), 669–683.

KIØRBOE, T., ANDERSEN, A., LANGLOIS, V. J., JAKOBSEN, H. H. & BOHR, T. 2009 Mechanisms and feasibility of prey capture in ambush-feeding zooplankton. *Proc. Natl Acad. Sci. USA* **106** (30), 12394–12399.

KIØRBOE, T., JIANG, H., GONÇALVES, R. J., NIELSEN, L. T. & WADHWA, N. 2014 Flow disturbances generated by feeding and swimming zooplankton. *Proc. Natl Acad. Sci. USA* **111** (32), 11738–11743.

KIØRBOE, T., TANG, K., GROSSART, H.-P. & PLOUG, H. 2003 Dynamics of microbial communities on marine snow aggregates: colonization, growth, detachment, and grazing mortality of attached bacteria. *Appl. Environ. Microbiol.* **69** (6), 3036–3047.

KOEHL, M. A. R. & STRICKIER, J. R. 1981 Copepod feeding currents: food capture at low Reynolds number. *Limnol. Oceanogr.* **26** (6), 1062–1073.

LAUGA, E. & POWERS, T. R. 2009 The hydrodynamics of swimming microorganisms. *Rep. Progr. Phys.* **72** (9), 096601.

LI, G., OSTACE, A. & ARDEKANI, A. M. 2016 Hydrodynamic interaction of swimming organisms in an inertial regime. *Phys. Rev.* E **94** (5), 053104.

MARTINDALE, J. D., JABBARZADEH, M. & FU, H. C. 2016 Choice of computational method for swimming and pumping with nonslender helical filaments at low Reynolds number. *Phys. Fluids* **28** (2), 021901.

MOLINA, J. J., NAKAYAMA, Y. & YAMAMOTO, R. 2013 Hydrodynamic interactions of self-propelled swimmers. *Soft Matt.* **9** (19), 4923–4936.

MORENO, R. D., LASERRE, A., BARROS, C. & OTHERS 2011 Protease activity involvement in the passage of mammalian sperm through the zona pellucida. *Biol. Res.* **44** (2), 145–150.

PAPAVASSILIOU, D. & ALEXANDER, G. P. 2017 Exact solutions for hydrodynamic interactions of two squirming spheres. *J. Fluid Mech.* **813**, 618–646.

PHAN-THIEN, N., TRAN-CONG, T. & RAMIA, M. 1987 A boundary-element analysis of flagellar propulsion. *J. Fluid Mech.* **184**, 533–549.

https://doi.org/10.1017/jfm.2018.509 Published online by Cambridge University Press

POTOMKIN, M., GYRYA, V., ARANSON, I. & BERLYAND, L. 2013 Collision of microswimmers in a viscous fluid. *Phys. Rev.* E **87** (5), 053005.

POZRIKIDIS, C. 2002 *A Practical Guide to Boundary Element Methods with the Software Library BEMLIB*. CRC Press.

RAMIA, M., TULLOCK, D. L. & PHAN-THIEN, N. 1993 The role of hydrodynamic interaction in the locomotion of microorganisms. *Biophys. J.* **65** (2), 755–778.

RIISGÅRD, H. U. & LARSEN, P. S. 2010 Particle capture mechanisms in suspension-feeding invertebrates. *Marine Ecol. Progr. Ser.* **418**, 255–293.

SHAIK, V. A. & ARDEKANI, A. M. 2017 Motion of a model swimmer near a weakly deforming interface. *J. Fluid Mech.* **824**, 42–73.

SMITH, D. J. 2009 A boundary element regularized Stokeslet method applied to cilia- and flagella-driven flow. *Proc. R. Soc. Lond.* A **465**, 3605–3626.

SOMMER, U., CHARALAMPOUS, E., GENITSARIS, S. & MOUSTAKA-GOUNI, M. 2017 Benefits, costs and taxonomic distribution of marine phytoplankton body size. *J. Plankton Res.* **39** (3), 494–508.

SPAGNOLIE, S. E., MORENO-FLORES, G. R., BARTOLO, D. & LAUGA, E. 2015 Geometric capture and escape of a microswimmer colliding with an obstacle. *Soft Matt.* **11** (17), 3396–3411.

STIMSON, M. & JEFFERY, G. B. 1926 The motion of two spheres in a viscous fluid. *Proc. R. Soc. Lond.* A **111** (757), 110–116.

STRICKLER, J. R. 1998 Observing free-swimming copepods mating. *Phil. Trans. R. Soc. Lond.* B **353** (1369), 671–680.

THEERS, M., WESTPHAL, E., GOMPPER, G. & WINKLER, R. G. 2016 Modeling a spheroidal microswimmer and cooperative swimming in a narrow slit. *Soft Matt.* **12** (35), 7372–7385.

https://doi.org/10.1017/jfm.2018.509 Published online by Cambridge University Press